

## SENSORS

# All-printed soft human-machine interface for robotic physicochemical sensing

You Yut, Jiahong Li†, Samuel A. Solomont†, Jihong Min, Jiaobing Tu, Wei Guo, Changhao Xu, Yu Song, Wei Gao\*

Ultrasensitive multimodal physicochemical sensing for autonomous robotic decision-making has numerous applications in agriculture, security, environmental protection, and public health. Previously reported robotic sensing technologies have primarily focused on monitoring physical parameters such as pressure and temperature. Integrating chemical sensors for autonomous dry-phase analyte detection on a robotic platform is rather extremely challenging and substantially underdeveloped. Here, we introduce an artificial intelligence-powered multimodal robotic sensing system (M-Bot) with an all-printed mass-producible soft electronic skin-based human-machine interface. A scalable inkjet printing technology with custom-developed nanomaterial inks was used to manufacture flexible physicochemical sensor arrays for electrophysiology recording, tactile perception, and robotic sensing of a wide range of hazardous materials including nitroaromatic explosives, pesticides, nerve agents, and infectious pathogens such as SARS-CoV-2. The M-Bot decodes the surface electromyography signals collected from the human body through machine learning algorithms for remote robotic control and can perform in situ threat compound detection in extreme or contaminated environments with user-interactive tactile and threat alarm feedback. The printed electronic skin-based robotic sensing technology can be further generalized and applied to other remote sensing platforms. Such diversity was validated on an intelligent multimodal robotic boat platform that can efficiently track the source of trace amounts of hazardous compounds through autonomous and intelligent decision-making algorithms. This fully printed human-machine interactive multimodal sensing technology could play a crucial role in designing future intelligent robotic systems and can be easily reconfigured toward numerous practical wearable and robotic applications.

## INTRODUCTION

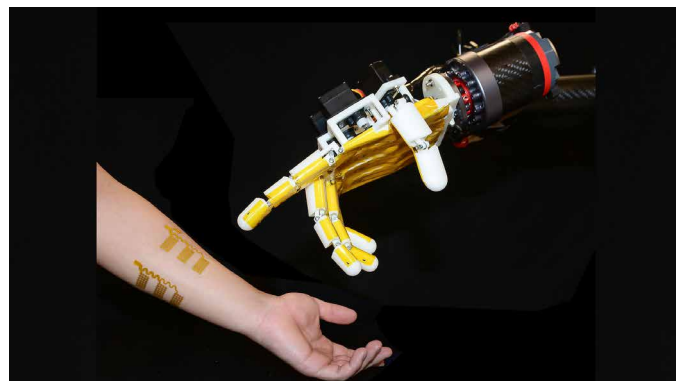
The development of advanced autonomous robotic systems that mimic and surpass human sensing capabilities is critical for environmental and agricultural protection as well as public health and security surveillance (1–4). In particular, robotic tactile perception allows for successful task implementation while avoiding harm to the device, user, and environment (4–6). In addition, autonomous trace-level threat detection prevents human exposure from toxic chemicals when operating in extreme and hazardous environments (7, 8). Such field-deployable, on-the-spot detection tools can be applied for the rapid identification of minute concentrations of nitroaromatic explosives that pose a health and security threat if they are unchecked (9–11). There are numerous toxic compounds that need to be tightly regulated in health and agriculture, such as organophosphates (OPs): pesticides or chemical warfare nerve agents that can cause neurological disorders, infertility, and even rapid death (12, 13). Such tools can be extended to monitor pathogenic biohazards such as SARS-CoV-2 without direct human exposure, which could play a crucial role in combating infectious diseases, especially because the current COVID-19 pandemic remains uncontrolled around the world (14–16). These strong demands for autonomous sensitive hazard detection have motivated the development of a controllable human-machine interactive robotic system with both physical and chemical sensing capabilities for task performing and point-of-use analysis.

Andrew and Peggy Cherng Department of Medical Engineering, Division of Engineering and Applied Science, California Institute of Technology, Pasadena, CA 91125, USA.

\*Corresponding author. Email: weigao@caltech.edu

†These authors contributed equally to this work.

Because of its high flexibility and conformability, electronic skin (e-skin) presents itself as the ideal interface between electronics and the human/robot bodies. In literature, e-skin has demonstrated a wide range of physical and chemical sensing applications, ranging from consumer electronics, digital medicine, smart implants, to environmental surveillance (17–31). Despite such promise, several challenges exist for e-skin-based multifunctional robotic systems. Because most rapid detection approaches for hazardous compounds require manual solution-based sample preparation steps, integrating chemical sensors for autonomous remote dry-phase analyte detection onto an e-skin-based robotic sensing platform is extremely challenging and substantially underdeveloped, hindering e-skin's capabilities for robotic interaction and cognition of the external world (7, 32). A robotic manipulator would require tactile, chemical, and



**Movie 1. Overview of the all-printed human-machine interface toward robotic physicochemical sensing.**

Copyright © 2022  
The Authors, some  
rights reserved;  
exclusive licensee  
American Association  
for the Advancement  
of Science. No claim  
to original U.S.  
Government Works

Downloaded from https://www.science.org at California Institute of Technology on June 27, 2022

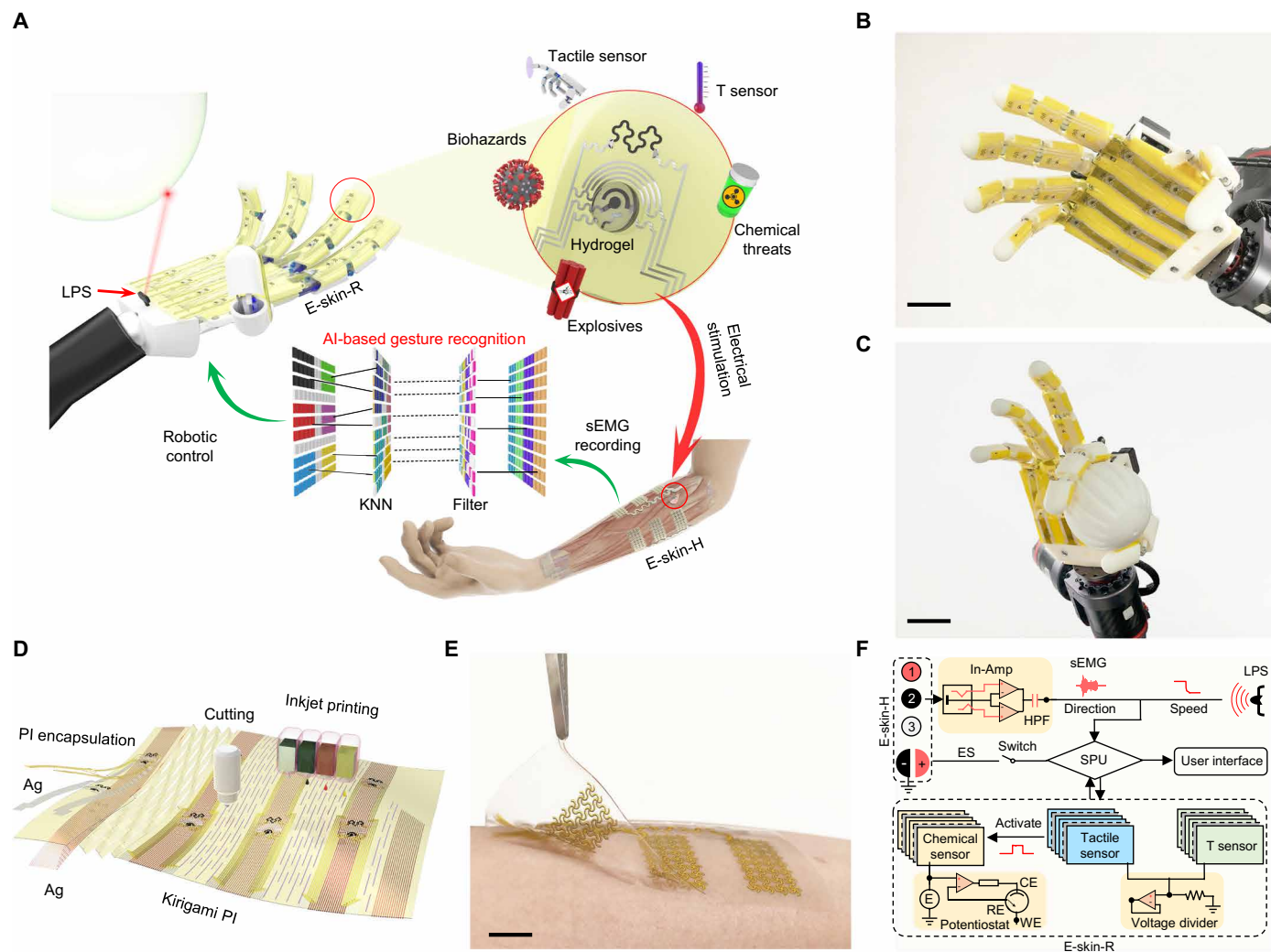


**Fig. 1. AI-powered M-Bot based on a fully printed soft human-machine interface.** (A) Schematic of the M-Bot that contains a pair of fully printed soft e-skins: e-skin-H (interfacing with the human skin) and e-skin-R (interfacing with the robotic skin) for AI-powered robotic control and multimodal physicochemical sensing with user-interactive feedback. *T*, temperature. (B and C) Photographs of the robotic skin-interfaced e-skin-R consisting of arrays of printed multimodal sensors. Scale bars, 3 cm. (D) Schematic illustration of rapid, scalable, and cost-effective prototyping of the kirigami soft e-skin-R using inkjet printing and automatic cutting. (E) Photograph of the human skin-interfaced soft e-skin-H with arrays of sEMG and feedback stimulation electrodes. Scale bar, 1 cm. (F) Schematic signal flow diagram of the M-Bot. In-Amp, instrumentation amplifier; HPF, high-pass filter; *E*, applied voltage; ES, electrical stimulation; SPU, signal processing unit. WE, CE, and RE represent working, counter, and reference electrodes of the printed chemical sensor, respectively.

temperature feedback to handle arbitrary objects, collect target samples, and carry out accurate chemical analysis in extreme environments (33). Another problem for e-skin interfaces is that preparing high-performance sensors generally requires manual drop-casting modifications of nanomaterials, which can lead to large sensor variations (34). Now, there is a lack of scalable low-cost manufacturing approaches to prepare thin, ultraflexible, multifunctional robotic physicochemical sensor patches. Despite these concerns, there is a strong need for an efficient human-machine interface that can reliably extract physiological features (35) as well as accurately control and receive real-time user-interactive feedback.

To address these challenges, we introduce here an artificial intelligence (AI)-powered human-machine interactive multimodal sensing robotic system (M-Bot) (Fig. 1A and Movie 1). The M-Bot is composed of two fully inkjet-printed stretchable e-skin patches,

namely, e-skin-R and e-skin-H, which interface conformally with the robot and human skin, respectively. The e-skins with powerful physicochemical sensing capabilities are mass producible and reconfigurable and can be entirely prepared using a high-speed, low-cost, and scalable inkjet-printing technology with a series of custom-developed nanomaterial inks. Upon collecting physiological data, the machine learning model can decode the surface electromyography (sEMG) signals from muscular contractions (recorded by e-skin-H) for robotic hand control. Simultaneously, e-skin-R can perform proximity sensing and tactile and temperature perceptual mapping, alongside real-time hydrogel-assisted electrochemical on-site sampling and analysis of both solution-phase and dry-phase threat compounds including explosives [such as 2,4,6-trinitrotoluene (TNT)], pesticides (such as OPs), and biohazards (such as SARS-CoV-2 virus). Upon detection, real-time haptic and threat alarm feedback communications were achieved via

electrical stimulation of the human body with e-skin-H. The threat sensing capabilities of the M-Bot could pave the way for automated chemical sensing, facilitating machine-mediated decisions for a wide range of practical robotic assistance applications.

## RESULTS

### Design of the human-machine interactive e-skins

E-skin-R is composed of high-performance-printed nanoengineered multimodal physicochemical sensor arrays that can be placed on the palm and fingers of the robotic hand (Fig. 1, B and C). The entire sensor patch can be rapidly manufactured in a large-scale and low-cost method via a powerful drop-on-demand inkjet printing technology (Fig. 1D, fig. S1, and movie S1). On top of e-skin-R are engraved kirigami structures that provide high stretchability without conductivity changes under a 100% strain, which is crucial for any robotic hand with high degrees of freedom in movement. E-skin-H consists of four sEMG electrode arrays (channels), alongside a pair of electrical stimulation electrodes, which can be fabricated similarly with inkjet printing followed by transfer printing onto a stretchable polydimethylsiloxane (PDMS) substrate (Fig. 1E). With assistance from AI, multimodal physicochemical sensing, and electrical stimulation-based feedback control, e-skin-R and e-skin-H form a closed-loop human-machine interactive robotic sensing system (Fig. 1F).

### Fabrication and characterization of the fully inkjet-printed multimodal sensor arrays

The multimodal physicochemical sensor arrays on e-skin-R were fabricated via serial printing of silver (interconnects and reference electrode), carbon (counter electrode and temperature sensor), polyimide (PI) (encapsulation), and target-selective nanoengineered sensing films (tactile sensor and biochemical sensing electrodes) (Fig. 2A). Customized nanomaterial inks were developed to meet the viscosity, density, and surface tension requirement for inkjet printing and to achieve the desired analytical performance (Figs. 2 and 3 and table S1). The chemical sensors were coated with a soft gelatin hydrogel that was loaded with an electrolyte or redox probe to facilitate target analyte sampling and analysis in situ (Supplementary Methods and fig. S4). The inkjet-printed carbon electrodes (IPCEs) showed reproducible electroanalytical performance and rapid response for on-site detection of dry-phase analytes (redox probe  $\text{Fe}^{3+}/\text{Fe}^{2+}$  was used in the hydrogel as an example) (fig. S5). The detection area or resolution can be enhanced by increasing either hydrogel size (fig. S6) or electrode density (fig. S7).

To effectively manipulate objects and to avoid harming either the e-skin or the object, real-time tactile feedback was enabled by incorporating a piezoresistive pressure sensor based on a printed silver nanowires (AgNWs)/nanotextured PDMS (N-PDMS) sensing film (Fig. 2, B and C). Such tactile sensation provides the robot with the haptic capability to grasp and handle samples. The geometry changes of the AgNWs/N-PDMS in response to a pressure load change the sensor's conductance (Fig. 2D and fig. S8). The pressure sensor displayed stable performance under repetitive pressure loading (Fig. 2E and fig. S8).

To demonstrate the feasibility of using the printed biosensors for hazardous chemical detection, a standard chemical explosive (TNT), an OP nerve agent simulant (paraoxon-methyl), and a biohazard pathogenic protein from the SARS-CoV-2 virus were chosen. The

detection of TNT was achieved using a Pt-nanoparticle-decorated graphene electrode, which was prepared by droplet inkjet printing of aqueous graphene oxide (GO), Pt ions, and propylene glycol and subsequently subjected to thermal reduction. The Pt-graphene showed superior electrocatalytic performance compared with classic carbon and graphene electrodes (Fig. 2, F to H, and fig. S9). The reduction of p-NO<sub>2</sub> to p-NH<sub>2</sub> catalyzed by the Pt-graphene can be detected via negative differential pulse voltammetry (nDPV) (9, 36). The obtained reduction peak amplitude in the nDPV voltammograms showed a linear relationship with the target TNT concentrations with a sensitivity of  $0.95 \mu\text{A cm}^{-2} \text{ppm}^{-1}$  and a detection limit of 10.0 ppm (Fig. 2I). Note that a custom voltammogram analysis with an automatic peak extraction strategy was used by the robot to analyze the original nDPV curves as illustrated in fig. S10. When integrated onto a robotic hand, the hydrogel-coated Pt-graphene sensor could sample the dry-phase TNT efficiently and provide a stable current response within 3 min (Fig. 2J); the TNT sensor can be regenerated in situ through repetitive nDPV scans to deplete the sampled analyte molecules toward continuous robotic sensing (fig. S11). For OP analysis, Pt-graphene and carbon have low electrochemical activity, because Zr-based metal-organic framework (MOF-808) was reported to have strong interaction with OPs (37, 38). Thus, the printed MOF-808-modified gold nanoparticle electrode (MOF-808/Au) was selected to achieve efficient non-enzymatic OP reduction at a relatively low voltage (Fig. 2, K to M, and fig. S12). In this way, the catalyzed reduction of paraoxon-methyl can be monitored via nDPV using the MOF-808/Au sensors with a sensitivity of  $1.4 \mu\text{A cm}^{-2} \text{ppm}^{-1}$  and a detection limit of 4.9 ppm (Fig. 2N). In addition to high sensitivity, these printed sensors could also perform high-concentration threat analysis (fig. S13). Similar to TNT detection, a 3- to 4-min sampling time was found to be sufficient for stable robotic dry-phase OP analysis (Fig. 2O). The Pt-graphene TNT sensors and MOF-808/Au OP sensors showed high selectivity over other nitro compounds (figs. S14 and S15). Because of the excellent stability of the catalytic performance of Pt-graphene and MOF-808/Au, the printed sensors can perform continuous TNT and OP analysis (fig. S16).

Label-free SARS-CoV-2 virus detection was demonstrated from a printed multiwalled carbon nanotube (CNT) electrode that was functionalized with antibodies specific to SARS-CoV-2 spike 1 protein (S1) (Fig. 2, P and Q). The CNT layer had a high electroactive surface area for sensitive electrochemical sensing while providing rich carboxylic acid functional groups for amine-containing affinity probe immobilization to achieve versatile biohazard sensing (39–41). The successful surface modification of the S1 sensor was confirmed after each surface immobilization step (Fig. 2R and figs. S17 and S18). Parts-per-billion level S1 sensing was performed on the basis of the signal change of the electroactive redox probe ( $\text{Fe}^{3+}/\text{Fe}^{2+}$ ) caused by the blockage of the electrode surface due to the S1 protein binding (Fig. 2S). The response variations of such S1 sensors can be further reduced in the future with an automatic surface modification process. The SARS-CoV-2 S1 sensor shows high selectivity over other viral proteins as illustrated in fig. S19. On-the-spot robotic S1 protein detection was successfully demonstrated using a collection and detection hydrogel containing the redox probe on the sensor that touched a surface containing a dry blot of the S1 protein (Fig. 2T). Although the nonspecific adsorption could potentially reduce the selectivity of the hydrogel detection process (fig. S20), the semiquantitative data conveniently and automatically



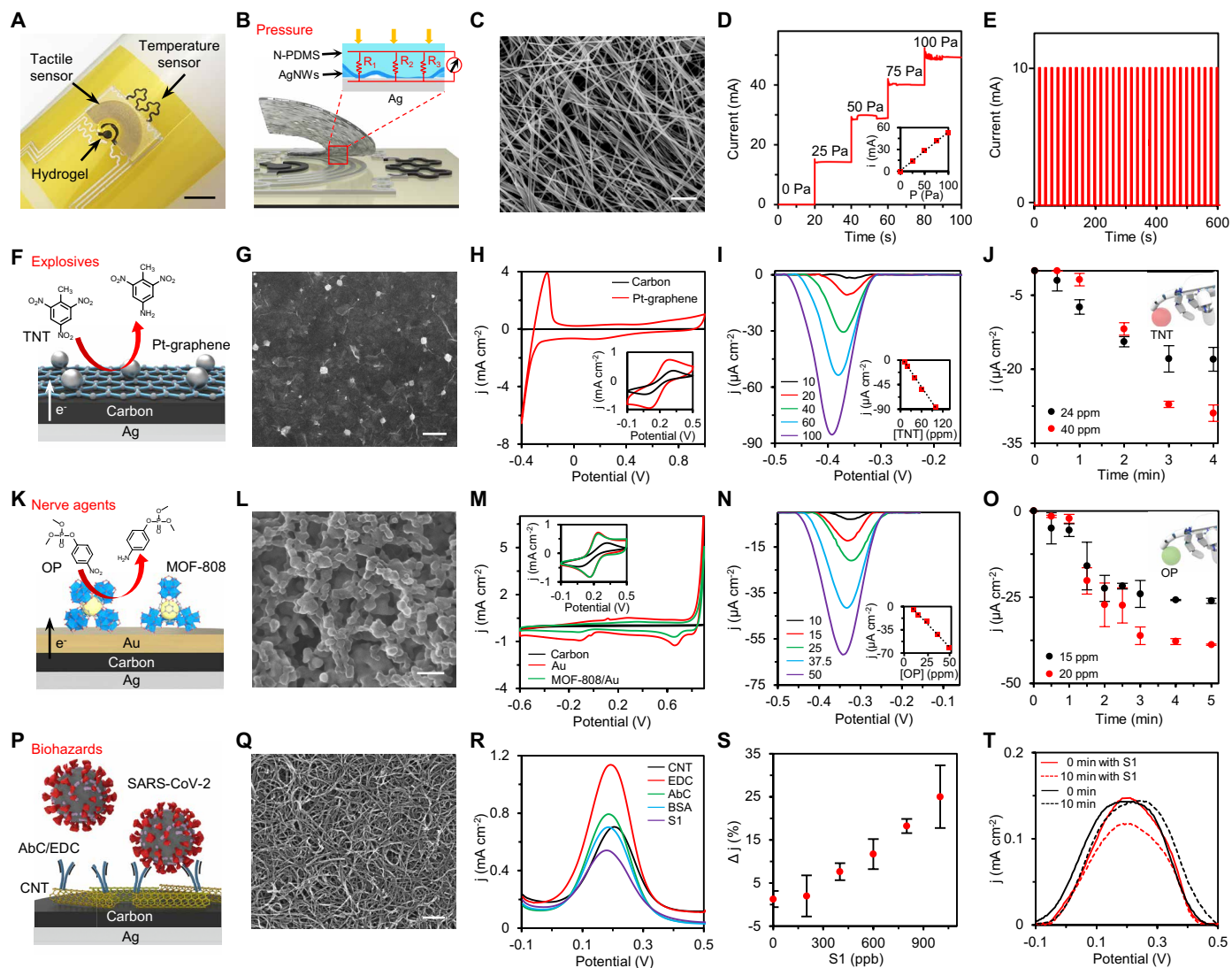


**Fig. 2. Characterization of the fully inkjet-printed multimodal sensor arrays on the e-skin-R.** (A) Photograph of a multimodal flexible sensor array printed with custom nanomaterial inks that consists of a temperature sensor, a tactile sensor, and an electrochemical sensor coated with a soft analyte-sampling hydrogel film. Scale bar, 5 mm. (B and C) Schematic (B) and SEM image (C) of the printed AgNWs/N-PDMS tactile sensor. Scale bar, 1  $\mu\text{m}$ . (D and E) Response of a tactile sensor under varied pressure loads (D) and repetitive pressure loading (E). (F and G) Schematic (F) and SEM (G) of the printed Pt-graphene electrode for TNT detection. Scale bar, 4  $\mu\text{m}$ . (H) Cyclic voltammograms (CVs) of an IPCE and a printed Pt-graphene electrode in 0.5 M  $\text{H}_2\text{SO}_4$  and in 5 mM  $\text{K}_3\text{Fe}(\text{CN})_6$  (inset).  $j$ , current density. (I) nDPV voltammograms and the calibration plots (inset) of TNT detection using a Pt-graphene electrode. (J) Dynamics of robotic fingertip detection of dry-phase TNT using a Pt-graphene sensor. (K and L) Schematic (K) and SEM image (L) of the printed MOF-808/Au electrode for OP detection. Scale bar, 100 nm. (M) CVs of an IPCE, a Au electrode, and a MOF-808/Au electrode in McIlvaine buffer and in 5 mM  $\text{K}_3\text{Fe}(\text{CN})_6$  (inset). (N) nDPV voltammograms of the OP detection. Inset: The calibration plots. (O) Robotic fingertip detection of dry-phase OP using a MOF-808/Au sensor. (P and Q) Schematic (P) and SEM image (Q) of the printed CNT electrode for SARS-CoV-2 detection. Scale bar, 250 nm. (R) DPV voltammograms of a printed CNT electrode in 5 mM  $\text{K}_3\text{Fe}(\text{CN})_6$  after each surface immobilization step. EDC, 1-ethyl-3-(3-dimethylammonopropyl)carbodiimide; AbC, capture antibody. (S) Calibration plots of the CNT-based sensor for S1 detection.  $\Delta j$ , percentage DPV peak current changes after target incubation. (T) Response of a CNT sensor in the presence and absence of dry-phase S1. All error bars represent the SD from three sensors.

obtained on site by the sensor could still provide the users rapid, real-time feedback and alert on the presence of biohazard.

To ensure accurate hazard detection in extreme operational environments, a printed carbon-based temperature sensor was designed for on-site temperature sensing and chemical sensor calibration during operation (fig. S21). All printed sensors maintained similar performance under and after repetitive mechanical bending tests, indicating their high mechanical stability (fig. S22). The freshly prepared hydrogels can be stored at 4°C in a moist chamber for

more than 1 week and maintain similar sensing performance (fig. S23). To minimize the influence of the shearing and normal forces on the sensor performance, the AgNWs/N-PDMS pressure sensor was designed to form a protection microwell for each hydrogel-coated biosensor and to facilitate reliable analyte sample collection (figs. S24 and S25); moreover, the tactile feedback from the AgNWs/N-PDMS pressure sensor could ensure stable electrochemical sensing performance (contact pressure was maintained between 0 and 500 Pa during operation).

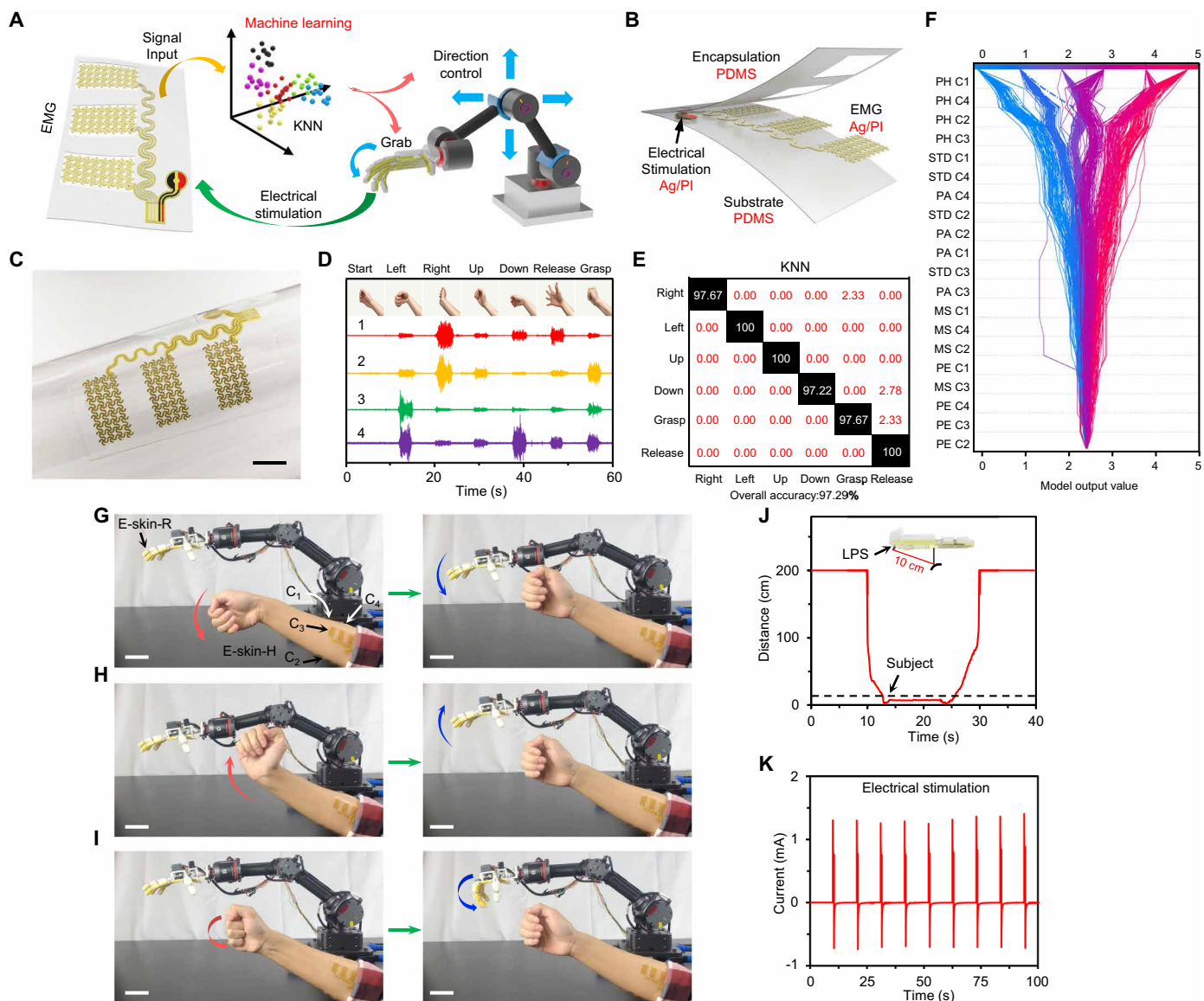


**Fig. 3. Evaluation of the e-skin-H for AI-assisted human-machine interaction.** (A) Schematic of machine learning-enabled human gesture recognition and robotic control. (B and C) Schematic (B) and photograph (C) of a PDMS encapsulated soft e-skin-H with sEMG and electrical stimulation electrodes for closed-loop human-interactive robotic control. Scale bar, 1 cm. (D) sEMG data collected by the four-channel e-skin-H from six human gestures. (E) Classification confusion matrix using a KNN model based on real-time experimental data. White text values, percentages of correct predictions; red text values, percentages of incorrect predictions. (F) A SHAP decision plot explaining how a KNN model arrives at each final classification for every data point using all five features. Each decision line tracks the features contributions to every individual classification; each final classification is represented as serialized integers (that map to a hand movement). Dotted lines represent misclassified points. (G to I) Time-lapse images of the AI-assisted human-interactive robotic control using the M-Bot. Scale bars, 5 cm. (J) Response of the LPS when the robot approaches and leaves an object. (K) Current applied on a participant's arm during the feedback stimulation.

### Evaluation of e-skin-H for AI-assisted human-machine interaction

E-skin-H acts as a human-machine interface for autonomous robotic control and object manipulation (Fig. 3A). In particular, e-skin-H records neuromuscular activity, which provides an intuitive interface to perform hand gesture recognition, through its inkjet-printed, PDMS-encapsulated, four-channel, three-electrode sEMG arrays (Fig. 3, B and C, and fig. S26, A to C). Analyzing the interfacial contact with the skin, e-skin-H demonstrates high stretchability with good mechanical compliance during physical activities through

its serpentine structure to provide reliable sEMG recordings (fig. S26, D to I).

Upon signal acquisition, various machine learning algorithms were evaluated for accurate gesture recognition including linear regression, random forest, artificial neural networks, support vector machines (kernels: radial, sigmoid, linear, and polynomial), and *k*-nearest neighbors (KNNs). Each algorithm was shown to extract motor intention from sEMG signals, acting as a bridge between conscious thought and prosthetic actuation. Of all the machine learning algorithms, the KNN model provided the highest prediction

accuracy for all six hand gestures with an overall mean accuracy across 5000 randomly selected training data of  $97.29 \pm 1.11\%$  based on real-time experimental results collected from a human participant (Fig. 3, D and E, and fig. S27). The next best model was the random forest classifier, which was found to have a similar average classification accuracy except with a higher variance. The KNN model was able to provide high-accuracy recognition of gestures with different angles when applying the e-skin-H to other body parts such as the neck, lower limb, and upper back—each time achieving an accuracy of greater than 90% (figs. S28 and S29).

For each gesture, five features were extracted from the associated peak in the root mean square (RMS)-filtered sEMG data (fig. S30): peak height (PH), peak standard deviation (STD), maximum slope (MS), peak average (PA), and peak energy (PE) (Supplementary Methods). The relevance of each feature and channel in the prediction method was further evaluated using Shapley additive explanation (SHAP) values (42). Through the SHAP values and the KNN accuracy, it was determined that PH was the most important feature for accurate gesture classification (Fig. 3F and fig. S31). When considered alongside PH, SD and PA both increased the classification accuracy, with SD being the most beneficial (figs. S31 and S32). In terms of channels, it was found that three EMG channels were sufficient to provide a high gesture accuracy of  $96.31 \pm 1.25\%$ . Adding a fourth channel was beneficial but not statistically significant (tables S2 and S3).

With the KNN algorithm, the robot can imitate the user's gesture in millisecond-level time for automatic object manipulation. The data acquisition and signal processing time delay to determine a gesture were around 200 ms, well below the required time for optimal real-time robotic control (43). This was achieved using a sampling rate of 534 Hz and analyzing the data in batches of 100 points. The M-Bot's time delay was substantially reduced by training the KNN model on only half of any sEMG signal for gesture recognition. By reducing the required data needed to determine a gesture, the machine learning model was able to predict the movement almost immediately after the gesture was complete.

The AI-powered e-skin-H-enabled gesture recognition provides a framework for online multidirectional robotic control with high-accuracy remote object manipulation (as illustrated in Fig. 3, G to I, and movie S2). After object contact, recognition, and positive threat detection, tactile and alarm feedback can be activated to inform the user of any potential danger using a pulsed current load between the two stimulation electrodes (Fig. 3J). To facilitate safe robotic handling and to protect e-skin-R from uncontrolled collisions, a laser proximity sensor was integrated into the robotic hand to reduce the actuation speed as the hand approaches a barrier (<10 cm) (Fig. 3K and fig. S33).

### Evaluation of the M-Bot in human-interactive robotic physicochemical sensing

With delicate and precise control, the human-machine interactive M-Bot was successfully evaluated for fingertip point-of-use robotic TNT detection (fig. S34 and movie S3). The multimodal sensor data could be captured in real time using a portable multichannel potentiostat, wirelessly transmitted to the mobile phone, and displayed on the cellphone app (fig. S34 and movie S3). The M-Bot was also able to perform object grasping and multipoint tactile and chemical sensing (Fig. 4, A to D, and movie S4). Multiplexed physicochemical data were simultaneously recorded and automatically processed without signal interferences (fig. S35). In an example demonstration, seven AI-assisted gesture-controlled steps were used in sequence to

control the robotic hand as it approached, grasped, and released a spherical object (Fig. 4E, fig. S36, and movie S4). In parallel, five sensor arrays were activated, displaying multiplexed tactile readings and surface TNT levels (Fig. 4, F and G).

The use of the M-Bot for multiplexed physicochemical robotic sensing was further evaluated on an OP-contaminated cylindrical surface (Fig. 4H). During the experiment, 14 sensor arrays on e-skin-R were activated. The tactile and OP sensor responses from each sensor, along with the corresponding color mapping of their distributions across the three-dimensional (3D) surface, are displayed in Fig. 4 (I and J, respectively) (detailed data are demonstrated in figs. S37 and S38). We anticipate that by further increasing the number and density of the multimodal sensor arrays, more accurate and informative data can be obtained from arbitrary objects and surfaces.

### Evaluation of an e-skin-R-enabled M-Boat for autonomous source tracking

The multimodal robotic sensing platform was further generalized onto an autonomous robotic boat capable of tracking pollutants, explosives, chemical threats, and biological hazards for risk prevention and mitigation, which is an important topic in civil security (7, 44). In this regard, our printed multimodal e-skin-R technology was adapted onto a multimodal sensing robotic boat (M-Boat) for real-time hazard detection and to autonomously locate the source of water-based chemical leakages (Fig. 5A). 3D printed from simple computer-aided designs, the M-Boat contains an inkjet-printed multimodal sensor array with one temperature and three chemical sensors, two electrical motors (for boat propulsion and steering), and a printed circuit board (PCB) for data collection, signal processing, and motor control (Fig. 5, B to D, and fig. S39). The propulsion of the M-Boat can be precisely controlled by adjusting the individual duty cycle of pulsed voltages supplied to each motor (Fig. 5E, fig. S40, and movie S5). For source detection, an  $A^*$  search algorithm (45) was implemented for autonomous decision-making while searching for the maximum concentration of the chemical leakage (Fig. 5, F and G, fig. S41, and Supplementary Methods). At each decision point, the sensors can detect small traces of the chemical leak in three equidistant locations around the boat. With this input, the algorithm calculates the optimal direction to travel using the gradient vector, indicating the direction of the highest concentration, and a heuristic estimate of the diffusion based on an interpolated map from previous points. By using the heuristic map in parallel with the gradient, the algorithm takes advantage of both the past and present results to precisely predict the spatial location of the source. The performance of the M-Boat was evaluated through simulations and experimentally in water tanks containing various chemical gradients induced by a low pH-corrosive fluid (Fig. 5, H and I, fig. S42, and movie S6) and OP leakage (Fig. 5, J and K). In the water tank, the M-Boat performed real-time detection of the surrounding analyte concentrations, automatically adjusting its trajectory based on the  $A^*$  algorithm, to successfully identify the leakage source. The M-Boat was also able to perform continuous hazard analysis and autonomous leakage tracking in seawater (fig. S43 and movie S6). The surrounding pH and ionic strength of a real-world sample matrix (e.g., lake water or seawater) did not show substantial influence on the sensor performance (fig. S44). When necessary, more real-time calibration mechanisms for precise hazard analysis can be introduced by incorporating more related biosensors (e.g., pH and



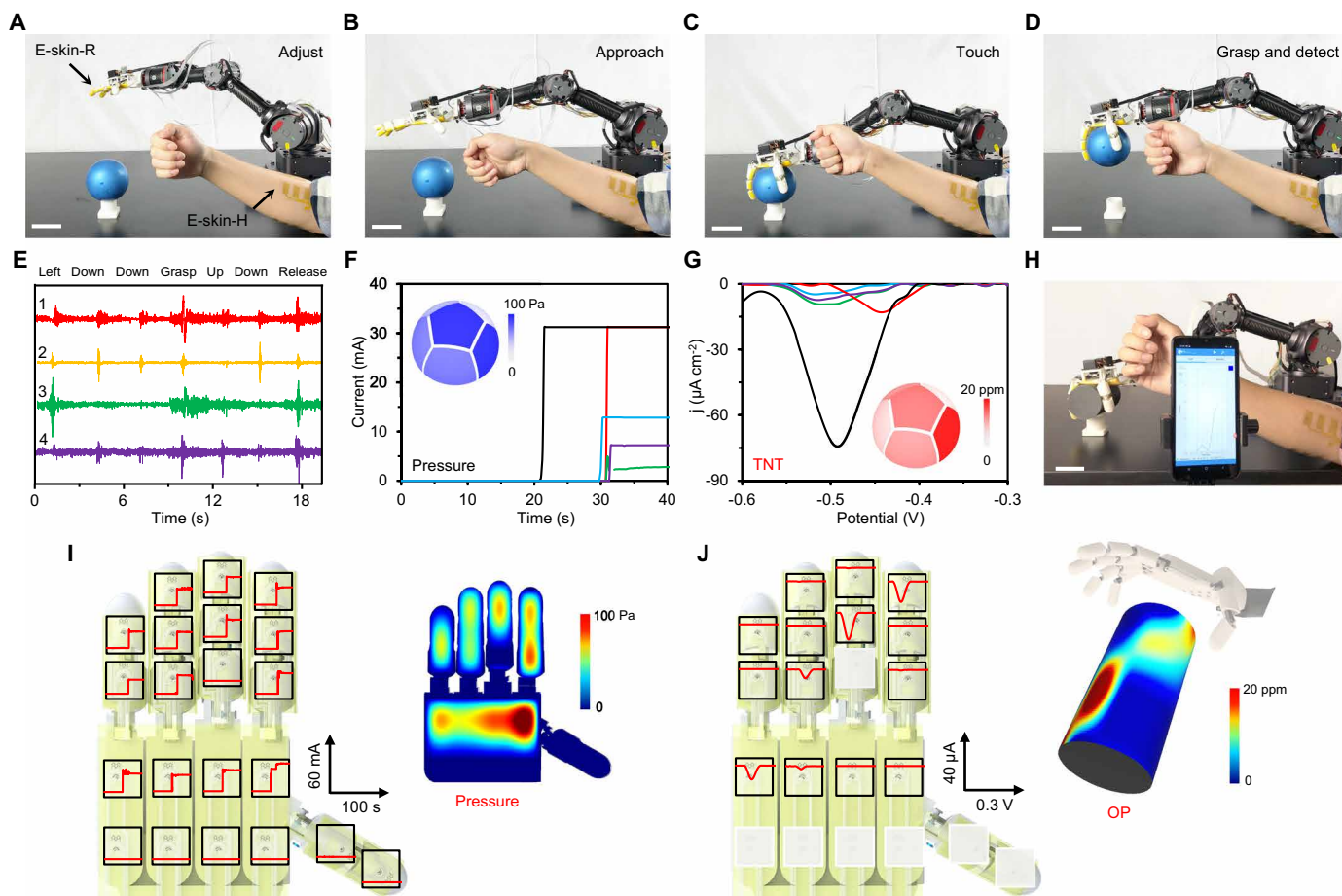


**Fig. 4. Evaluation of the M-Bot in human-interactive robotic physicochemical sensing.** (A to D) Time-lapse images of the human-interactive robotic control for object grasping and on-site TNT detection. Scale bars, 5 cm. (E to G) The sEMG data collected in real time, which allow the robotic hand to approach and grasp a spherical object (E) and the corresponding tactile (F) and TNT (G) sensor responses. Insets in (F) and (G) represent the colored mapping of pressure and TNT distributions on the object. (H to J) Photograph of the robotic OP sensing on a cylindrical object (H) and the corresponding responses of the tactile sensors (I) and OP sensors (J) on an e-skin-R. Insets in (I) and (J) represent the color mappings of pressure and OP distributions on the object. Scale bar, 5 cm.

conductivity sensors) into the e-skin-R. With more advanced robotic control and sensing designs, the M-Boat platform could serve as an important basis for intelligent path planning and decision-making of autonomous vehicles.

## DISCUSSION

Here, we have described a human-machine interactive e-skin-based robotic system (M-Bot) with multimodal physicochemical sensing capabilities. The mass-producible flexible sensor arrays allow for high-performance on-site monitoring of temperature, tactile pressure, and various hazardous chemicals (in both dry phase and liquid phase) such as explosives, OPs, and pathogenic proteins. The integration of such multimodal sensors onto a robotic e-skin platform provides autonomous systems with interactive cognitive capabilities and substantially broadens the range of tasks that robots can perform, such as combating infectious diseases like COVID-19.

Existing robotic sensing technologies are largely limited to monitoring physical parameters such as temperature and pressure. To achieve high-performance chemical sensing, nanomaterials are commonly

used via manual drop-casting methods, which could lead to large sensor variations. Moreover, most electrochemical sensing strategies require detection in aqueous solutions, making them impractical for dry-phase robotic analysis. Now, there are no reported scalable low-cost manufacturing approaches to prepare robotic physicochemical sensors. In this work, we proposed a scale solution to fabricate flexible, multifunctional, and multimodal sensor arrays prepared entirely by high-speed inkjet printing. Custom-developed functional nanomaterial inks are designed and optimized to achieve highly sensitive and selective sensors for the specific hazardous target analytes. The hydrogel-coated printed nanobiosensors allow for efficient dry-phase chemical sampling and rapid on-site hazard analysis on a robotic platform.

Manufactured using the same approach, e-skin-H ensured stable contact with the soft human skin for reliable recording of neuromuscular activity to facilitate remote robotic sensing and control. To minimize the amount of data collected and analyzed for human-robotic interaction, AI and smart algorithms were applied to decode incoming information and efficiently predict and control robotic movement. An in-depth analysis into each sEMG channel's individual

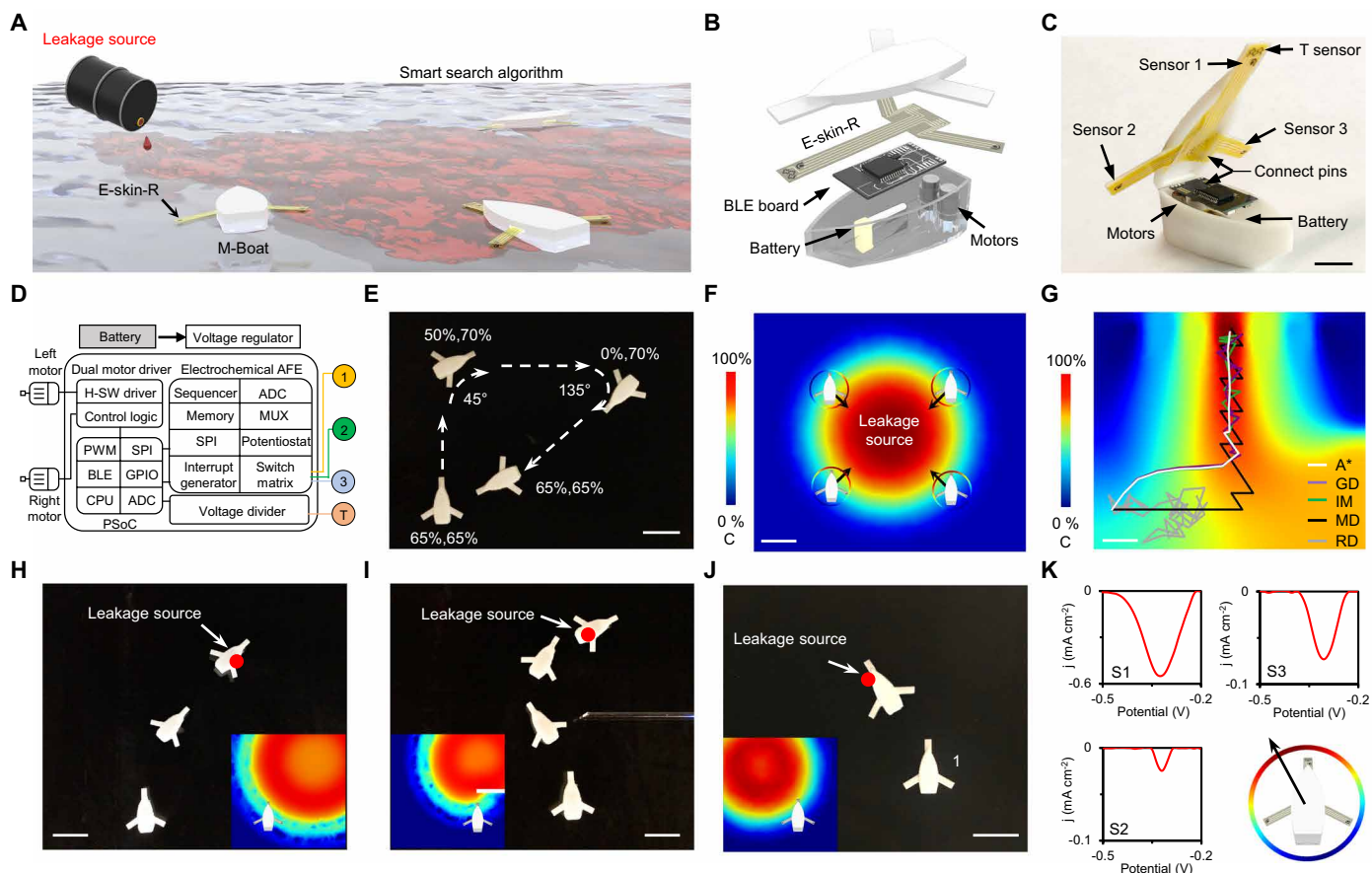


**Fig. 5. Evaluation of the-skin-R in an autonomous M-Boat.** (A) Schematic of the intelligent M-Boat integrated with a printed multimodal e-skin-R sensor array that can perform temperature and multiplexed chemical sensing for autonomous source tracking. (B and C) Schematic (B) and photograph (C) illustrating the assembly of the M-Boat components. (D) System block diagram of the M-Boat for autonomous propulsion, sensing, and signal processing. AFE, analog front end; CPU, central processing unit; H-SW, H-bridge software; MUX, multiplexer. (E) Wireless control of the M-Boat. (F) Simulated distributions of a hazardous chemical (OP) leak and the algorithm used by the M-Boat for autonomous source tracking. C, concentration. (G) Simulation comparison of different search algorithms used by the M-Boat for intelligent source tracking. GD, gradient descent; IM, interpolated map; MD, max direction; RD, random direction. (H and I) Time-lapse images showing example demonstrations of the M-Boat-enabled autonomous source tracking. Insets: Simulated target (proton from corrosive acid) distributions. Scale bars, 5 cm. (J and K) Time-lapse images (J) and the nDPV voltammograms collected at location 1 (K) for autonomous decision-making and chemical threat (OP) source tracking using an M-Boat. Insets: Simulated OP distribution. Scale bar, 5 cm.

contribution to the machine learning model was presented, allowing future researchers to optimize the number of electrodes needed for robotic control. Using the SHAP analysis, we further untangled the hidden overlapping information between each channel's features and categorized which features present the most nonoverlapping information for gesture prediction. For the M-Bot, machine learning gesture prediction via e-skin-H was further coupled with user-interactive tactile and threat alarm feedback that allow seamless human-machine interaction for the remote deployment of robotic technology in extreme or contaminated environments. To obtain such real-time results, the robotic platform's data acquisition, signal processing, feature extraction, and gesture prediction of the sEMG signals were performed with millisecond-level time after the gesture was complete. The M-Boat similarly used a smart A\* algorithm for autonomous source detection, minimizing the boat's path, and subsequently, time and energy, in finding potentially hazardous chemical leaks. In these applications, the systems demonstrated real-time autonomous movement, all within a low-cost mass-producible system, lowering the barrier for real-time robotic perception.

This human-machine-interactive robotic sensing technology represents an attractive approach to develop advanced flexible and soft e-skins that can reliably collect vital data from the human body and the surrounding environments. Full system integration to achieve high-speed, wireless, and simultaneous multichannel physico-chemical sensing is strongly desired for future field deployment and evaluation. Moreover, we envision that, by integrating a high density and new types of multimodal sensors, this technology could substantially enhance the perceptual capabilities of future intelligent robots and pave the way to numerous new practical wearable and robotic applications.

## MATERIALS AND METHODS

### Materials

Graphite flake was purchased from Alfa Aesar. Sodium nitrate, potassium permanganate, hydrogen peroxide, potassium hexacyanoferrate(III), citric acid, chloroplatinic acid, PDMS, zirconium(IV) chloride, aniline, gelatin, paraoxon-methyl, TNT solution, 4-nitrophenol, 2-nitrophenyl



octyl ether, 2-nitroethanol, 2-nitropropane, 4-nitrotoluene, 2,4-dinitrotoluene, poly(pyromellitic dianhydride-co-4,4'-oxydianiline) amic acid (PAA) solution [12.8 weight % (wt %)], 1-methyl-2-pyrrolidinone (NMP), *N*-hydroxysulfosuccinimide sodium salt (Sulfo-NHS), *N*-(3-dimethylaminopropyl)-*N'*-ethyl carbodiimide hydrochloride (EDC), 2-(*N*-morpholino)ethanesulfonic acid hydrate (MES), potassium permanganate (KMnO<sub>4</sub>), bovine serum albumin (BSA), human immunoglobulin G (IgG), and lysozyme were purchased from Sigma-Aldrich. Sodium chloride, sulfuric acid, hydrochloric acid, disodium phosphate, 1,3,5-benzenetricarboxylic acid (H<sub>3</sub>BTC), formic acid, *N,N'*-dimethylformamide (DMF), potassium ferricyanide, propylene glycol, isopropyl alcohol (IPA), and phosphate-buffered saline (PBS) were purchased from Thermo Fisher Scientific. His-tagged SARS-CoV-2 S1 (PNA002), anti-Spike-RBD human monoclonal antibody (IgG) (S1-IgG, AHA013), SARS-CoV S1 (40150-V08B1), SARS-CoV nucleocapsid protein (NP; 40143-V08B), and SARS-CoV-2 NP (40588-V08B) were purchased from Sanyou Biopharmaceuticals. AgNW suspension (20 mg ml<sup>-1</sup> in IPA) was purchased from ACS Material LLC. Silver ink (25 wt %) and carbon ink (5 wt %) were purchased from NovaCentrix. Gold ink (10 wt %) was purchased from C-INK Co. Ltd. Carboxyl-functionalized multiwalled CNT ink (2 mg ml<sup>-1</sup>; Nink-1000) was purchased from NanoLab Inc. PI film (12.5 μm) was purchased from DuPont.

### Preparation and characterizations of print inks

To prepare the Pt-graphene ink, GO was first prepared following a modified Hummer's method (46). One gram of graphite flake was mixed with 23 ml of H<sub>2</sub>SO<sub>4</sub> for more than 24 hours, and then 100 mg of NaNO<sub>3</sub> was added inside. Subsequently, 3 g of KMnO<sub>4</sub> was added below 5°C in an ice bath. After stirring at 40°C for another 30 min, 46 ml of H<sub>2</sub>O was added while the solution temperature was slowly increased to 80°C. In the end, 140 ml of H<sub>2</sub>O and 10 ml of H<sub>2</sub>O<sub>2</sub> were introduced into the mixture to complete the reaction. The GO was washed with 1 M HCl and filtered. After dried under vacuum at 60°C, a GO (2 mg ml<sup>-1</sup>) suspension was prepared followed by the addition of 5 mM chloroplatinic acid under sonication. Last, the suspension was mixed with propylene glycol (80:20, v/v) to form the Pt-graphene ink.

The MOF-808 was synthesized solvothermally. Briefly, H<sub>3</sub>BTC (0.236 mM) and ZrCl<sub>4</sub> (1 mM) were mixed with 15.6 ml of the DMF and formic acid (1:0.56, v/v) solvent and sonicated for 20 min. Then, the mixture was transferred to a 25-ml Teflon-lined autoclave and kept at 120°C for 12 hours. After the reaction, the autoclave was naturally cooled to room temperature. The product was washed with DMF and methanol and then dried under vacuum at 60°C. Last, a MOF-808 suspension in deionized (DI) water was prepared and mixed with propylene glycol (80:20, v/v) to form the MOF-808 ink.

The AgNWs ink was prepared by diluting the AgNW suspension with IPA to 2 mg ml<sup>-1</sup> and sonicating it for 10 min. The CNT ink was prepared by mixing the commercial CNT ink (2 mg ml<sup>-1</sup>) with propylene glycol (80:20, v/v). PAA ink was prepared by diluting the commercial PAA solution with NMP to 3 wt %. Commercial silver and carbon inks were used as received.

The dynamic viscosity ( $\eta$ ), density ( $\rho$ ), and surface tension ( $\gamma$ ) for all inks were characterized before printing. Dynamic viscosity was characterized with an Anton Paar MCR302 rheometer. Surface tension was measured with a Ramé-Hart contact angle goniometer using the equation

$$\gamma = \Delta\rho g R_0^2 / \beta \quad (1)$$

Here,  $\Delta\rho$  is the density difference between air and inks,  $g$  is the gravitational acceleration,  $R_0$  is the radius of curvature at the drop apex, and  $\beta$  is the shape factor.

### Fabrication and assembly of the soft inkjet-printed e-skin-R

The fabrication process of the inkjet-printed e-skin-R is illustrated in fig. S1. The PI substrate was cut with kirigami structures by automatic precision cutting (Silhouette Cameo 3). A 2-min O<sub>2</sub> plasma surface treatment was performed with Plasma Etch PE-25 (10 to 20 cm<sup>3</sup> min<sup>-1</sup> O<sub>2</sub>, 100 W, 150 to 200 mtorr) to enhance the surface hydrophilicity of the PI substrate. The multimodal sensor arrays on e-skin-R were fabricated via serial printing of silver (interconnects and reference electrode), carbon (counter electrode and temperature sensor), PI (encapsulation), and target-selective nanoengineered sensing layers (e.g., AgNWs, Pt-graphene, Au, and MOF-808) using an inkjet printer (DMP-2850, Fujifilm). The ink composition, characterizations, and thermal annealing conditions are shown in table S1. Thirty layers of AgNWs were printed on an N-PDMS substrate (cured on a 1000-mesh sandpaper) to form the piezoresistive tactile sensors. While printing, the plate temperature was set to 40°C to ensure the rapid vaporization of the IPA solvent. The AgNWs/N-PDMS were cut to semicircle shape and set on the e-skin.

For preparing biohazard S1 protein sensor (fig. S17), a CNT film was printed on the IPCE first. The carboxylic groups of multiwall CNTs were activated to NHS esters, by drop-casting 10 μl of EDC (400 mM) and NHS (100 mM) in MES buffer (25 mM, pH 5) for 35 min. In the next step, 5 μl of anti-Spike-RBD antibody (250 μg ml<sup>-1</sup>) in PBS were dropped on the modified electrode and incubated for 2 hours. Next, 10 μl of 1% BSA in PBS were dropped and incubated for 1 hour to deactivate residual NHS esters. The modified sensors were stored in the refrigerator until use.

To assemble the robotic e-skin, the pins of the finger printed e-skin were connected with the bottom printed silver connections of palm part through a  $z$  axis conductive tape (3M), and then e-skin-R was set on a robotic hand printed with a 3D printer (Mars Pro, Elegoo Inc.).

### Characterizations of the multimodal robotic sensing performance of e-skin-R

The printed biosensors were characterized with cyclic voltammetry (scan rate: 50 mV s<sup>-1</sup>, unless otherwise noted), DPV, and amperometric current ( $i$ )-time ( $t$ ) through an electrochemical workstation (CHI 660E). McIlvaine buffer solutions (pH 6.0) were used to prepare the analyte solutions. A commercial Ag/AgCl reference electrode (CHI111) was used for characterizing the printed sensing electrodes in the solution, whereas printed Ag solid-state electrodes were used for hydrogel-based sensor characterization (there was an ~0.1-V difference between these two types of reference electrodes in McIlvaine buffer). To quantify the electrochemical performance and the electrochemical surface areas, the print electrodes were tested in 5 mM K<sub>3</sub>Fe(CN)<sub>6</sub> and 1 M KCl with scan rates of 5 mV s<sup>-1</sup> from -0.1 to 0.5 V.

For TNT and OP sensors, the conditions of nDPV measurements include a scan range of -0.15 to -0.5 V, an incremental potential of 0.004 V, a pulse amplitude of 0.05 V, a pulse width of 0.05 s, and a pulse period of 0.5 s. The reduction peaks of nDPV curves were extracted using a custom-developed iterative baseline correction

algorithm. To prepare the electrolyte-loaded hydrogel for analyte sampling and sensing, 0.250 g of gelatin powder, 0.075 g of KCl, 0.071 g of citric acid, and 0.179 g of disodium phosphate were mixed in 10 ml of DI water and stirred at 80°C for 15 min. The hydrogel was stored and aged overnight. The gelatin electrolyte-loaded hydrogel was coated on the printed biosensors for dry blot detection.

For S1 protein detection, the modified electrode was incubated with 10  $\mu\text{l}$  of S1 protein in PBS for 10 min, and the DPV measurements ranged from  $-0.1$  to  $0.5$  V. The electrochemical signal of the sensor before and after antigen binding was measured in 5 mM  $\text{K}_3\text{Fe}(\text{CN})_6$ . The difference between the peak current densities ( $\Delta j$ ) was obtained as sensor readout. A sampling hydrogel pad was prepared to demonstrate the feasibility for SAR-CoV-2 virus dry blot detection. To perform one-step detection, 10  $\mu\text{l}$  of gelatin hydrogel [7.5 wt % gelatin, 10 mM  $\text{K}_3\text{Fe}(\text{CN})_6$ , and 0.2 M phosphate buffer (pH 7.0)] was placed onto a dry S1 protein blot [from 10  $\mu\text{l}$  of a SARS-CoV-2 S1 protein droplet (1  $\mu\text{g ml}^{-1}$ )]. Such amount of S1 protein could potentially be found in the saliva droplet of a patient with COVID-19 (47). For dry-phase sensing selectivity study, the dry protein blots were created with the same amount of interference proteins (10  $\mu\text{l}$ , 1  $\mu\text{g ml}^{-1}$ ). The electrochemical signal of the gel was recorded immediately and 10 min after joining the biosensor with the gel.

The temperature sensor characterization was performed on a ceramic hot plate (Thermo Fisher Scientific), and an amperometric method (with an applied voltage of 2 V) was used to detect the temperature response. The piezoresistive tactile sensor characterization was also applied with a constant voltage of 2 V to record the current response under various pressure loads.

The scanning electron microscopy (SEM) images of the electrodes were obtained by a field-emission SEM (FEI Nova 600 NanoLab). Energy-dispersive spectroscopy (EDS) mapping were obtained by an EDS spectrometer (Bruker Quantax EDS).

### Fabrication and assembly of e-skin-H

The fabrication process of e-skin-H was illustrated in fig. S26. A 2-min  $\text{O}_2$  plasma surface treatment was performed with Plasma Etch PE-25 to enhance the surface hydrophilicity of the PI substrate. Silver interconnects were printed with DMP-2850. The PI substrate without the printed patterns were removed with laser cut using a 50-W  $\text{CO}_2$  laser cutter (Universal Laser Systems). The optimized laser cutter parameters were power of 10%, speed of 80%, and pixels per inch (PPI) of 1000 in vector mode. After cleaned with ethanol and dried, the remaining patterns were transferred onto a 70- $\mu\text{m}$ -thick PDMS substrate and then encapsulated with another layer of PDMS film as well (with sEMG and electrical stimulation electrodes exposed). An adhesive electrode gel (Parker Laboratories Inc.) was spread onto the electrodes before placing on human participants.

### Evaluation of the human-machine interactive multimodal sensing robot

To evaluate the performance of the M-Bot, the e-skin-R–interfaced 3D printed robotic hand was assembled onto a five-axis robotic arm (Innfo Ltd.). The e-skin-H was then set around a human participant's forearm after cleaning the skin with alcohol swabs. The sEMG data were acquired with four channels (three sEMG electrodes in each channel) through an open-source hardware shield (Olimex). The signals were sampled as integers between 0 and 1023 by a 10-bit analog-to-digital converter (ADC) and then processed through a serial (cluster communication) port. Each channel was then scaled

back into voltages between 0 and 5 V. Although the robotic arm control was performed in real time, data processing was performed asynchronously to signal acquisition. During processing, the data were first put through a high-pass filter with a cutoff frequency of 100 Hz. The points were subsequently downsized using an RMS filter (batch size: 400 points and step size: 10 points). The peaks detected after processing were used as features for the machine learning model. Overlapping peaks from each channel (peaks within a half-peak width away) were categorized as a single group. If multiple peaks were detected in a single channel's set, then the first peak was used. The KNN training model was built using 60 samples per each of the six gestures. The training and testing datasets were divided 2:1, respectively, and were randomly selected using an equal representation of each gesture. After the model was developed, it was further evaluated for accuracy using new data from each gesture. The laser proximity sensor (LPS) (TOF10120) was operated through a customized interactive control software in Python (Python 3.8). For dry blot threat detection, TNT and OP threat coatings were created by spraying analyte vapor onto the selected objects in a fume hood. Multimodal sensing data collected during robotic sensing operations were collected through a portable electrochemical workstation (PalmSens4) with a multiplexer.

The validation and evaluation of the M-Bot were performed using human participants in compliance with all the ethical regulations under protocols (ID 19-0895) that were approved by the Institutional Review Board at the California Institute of Technology. Three participants were recruited from the California Institute of Technology's campus and the neighboring communities through advertisement. All participants gave written informed consent before study participation.

### Machine learning data analysis

For each gesture, all five features were extracted from the associated peak in the RMS-filtered EMG data: height, average area, SD, average energy (intensity), and maximum slope. The features extracted were calculated in reference against their baselines, which were determined via a binary search of the previous data in 50-ms intervals.

After feature extraction, SHAP values were used to evaluate the performance enhancement of each feature extracted and EMG channel used. In addition to SHAP values, the average testing accuracy across 5000 training sessions was taken for each permutation of features and EMG channels, which supplemented the SHAP values in providing further insight into which channels and features contained nonoverlapping beneficial information for gesture determination. For each of the 5000 trials, the testing points represented 33% of the dataset, with each gesture in the test set being proportionally represented in the full dataset. For the arm EMG dataset, this amounted to 387 movements split across six gestures; of those points, the KNN model was fit using 257 training points and scored on the remaining 128 testing points (testing and training were proportionally stratified across all six gestures).

### Evaluation of the M-Boat

To evaluate the performance of the M-Boat, the e-skin-R was assembled onto a 3D printed boat with a four-layer PCB, as shown in Fig. 5 (B and C). On the PCB, a Bluetooth low-energy (BLE) module (CYBLE-222014-01, Cypress Semiconductor) was used for controlling the electrochemical front end through a serial peripheral interface (SPI). This module was also used to control the motor

driver through general purpose input/output (GPIO) pins and pulse width modulation (PWM) and to transmit data over BLE. An electrochemical front end (AD5941, Analog Devices) was set up via SPI to perform multiplexed electrochemical measurements with the sensor arrays and to send the acquired data to the BLE module for signal processing and BLE transmission. A BLE dongle (CY5677, Cypress Semiconductor) was used to establish a BLE connection with the M-Boat and to securely receive the sensor data via BLE indications. An A\* algorithm was used to analyze the sensor data and compute the next M-Boat's movement path with the optimal motor speed. The calculated motor speed information was sent back to the BLE module in real time for the pulse width-modulated control of two motors (Q4SL2BQ280001) through a dual dc motor driver (TB6612FNG, Toshiba). The entire system was powered by a 3.7-V Li-ion battery (40 mAh).

For the OP chemical threat tracking experiment, a natural diffusion gradient was generated by 10 droppings of 20  $\mu\text{l}$  of 0.1 M OP into a 0.1 M NaCl solution tank. The seawater studies were performed in seawater samples collected from the Pacific Ocean in Los Angeles. The M-Boat was set into the tank after 30 min. For the corrosive acidic threat tracking experiment, pH sensors were modified on e-skin-R instead. Briefly, a polyaniline pH-sensitive film was electropolymerized on the IPCE in a solution containing 0.1 M aniline and 0.1 M HCl using a CV from  $-0.2$  to  $1$  V for 25 cycles at a scan rate of  $50$  mV s $^{-1}$ . Then, 100  $\mu\text{l}$  of H $_2$ SO $_4$  (2 M) as the leakage source was dropped into the middle of the water tank. Last, the M-Boat was set after 45/30 min with/without barriers in the tank, respectively.

## Statistical analysis

All quantitative values were presented as means  $\pm$  SD of the mean. For all sensor evaluation plots, the error bars were calculated on the basis of the SD from three sensors. For the hydrogel stability study, the error bars were calculated on the basis of the SD from three hydrogels. For bending tests of the sEMG electrodes, the error bars were calculated on the basis of the SD from three independent measurements. For the machine learning analysis of the sEMG data, the model was trained on the same data across 5000 trials of randomly splitting the points between training and testing data. The accuracy profile of this training was then fit to a skewed normal distribution, where the mean was extracted.

## SUPPLEMENTARY MATERIALS

[www.science.org/doi/10.1126/scirobotics.abn0495](http://www.science.org/doi/10.1126/scirobotics.abn0495)

Methods

Figs. S1 to S44

Tables S1 to S3

Movies S1 to S6

[View/request a protocol for this paper from Bio-protocol.](#)

## REFERENCES AND NOTES

- G.-Z. Yang, J. Bellingham, P. E. Dupont, P. Fischer, L. Floridi, R. Full, N. Jacobstein, V. Kumar, M. McNutt, R. Merrifield, B. J. Nelson, B. Scassellati, M. Taddeo, R. Taylor, M. Veloso, Z. L. Wang, R. Wood, The grand challenges of Science Robotics. *Sci. Robot.* **3**, eaar7650 (2018).
- S. Sundaram, P. Kellnhofer, Y. Li, J.-Y. Zhu, A. Torralba, W. Matusik, Learning the signatures of the human grasp using a scalable tactile glove. *Nature* **569**, 698–702 (2019).
- M. Cianchetti, C. Laschi, A. Mencias, P. Dario, Biomedical applications of soft robotics. *Nat. Rev. Mater.* **3**, 143–153 (2018).
- A. Chortos, J. Liu, Z. Bao, Pursuing prosthetic electronic skin. *Nat. Mater.* **15**, 937–950 (2016).
- C. M. Boutry, M. Negre, M. Jorda, O. Vardoulis, A. Chortos, O. Khatib, Z. Bao, A hierarchically patterned, bioinspired e-skin able to detect the direction of applied pressure for robotics. *Sci. Robot.* **3**, eaau6914 (2018).
- J. Yin, R. Hinchet, H. Shea, C. Majidi, Wearable soft technologies for haptic sensing and feedback. *Adv. Funct. Mater.* **31**, 2007428 (2020).
- H. Ishida, Y. Wada, H. Matsukura, Chemical sensing in robotic applications: A review. *IEEE Sens. J.* **12**, 3163–3173 (2012).
- J. Trevelyan, W. R. Hamel, S.-C. Kang, in *Springer Handbook of Robotics*, B. Siciliano, O. Khatib, Eds. (Springer International Publishing, Cham, 2016), pp. 1521–1548.
- W. Wang, Electrochemical sensing of explosives. *Electroanalysis* **19**, 415–423 (2007).
- S. Singh, Sensors—An effective approach for the detection of explosives. *J. Hazard. Mater.* **144**, 15–28 (2007).
- A. Fainberg, Explosives detection for aviation security. *Science* **255**, 1531–1537 (1992).
- S. Vucinic, B. Antonijevic, A. M. Tsatsakis, L. Vassilopoulou, A. O. Docea, A. E. Nosyrev, B. N. Izotov, H. Thiermann, N. Drakoulis, D. Brkic, Environmental exposure to organophosphorus nerve agents. *Environ. Toxicol. Pharmacol.* **56**, 163–171 (2017).
- J. Bajgar, Organophosphates/nerve agent poisoning: Mechanism of action, diagnosis, prophylaxis, and treatment. *Adv. Clin. Chem.* **38**, 151–216 (2004).
- A. Gao, R. R. Murphy, W. Chen, G. Dagnino, P. Fischer, M. G. Gutierrez, D. Kundrat, B. J. Nelson, N. Shamsudhin, H. Su, J. Xia, A. Zemmar, D. Zhang, C. Wang, G.-Z. Yang, Progress in robotics for combating infectious diseases. *Sci. Robot.* **6**, eabf1462 (2021).
- Y. Shen, D. Guo, F. Long, L. A. Mateos, H. Ding, Z. Xiu, R. B. Hellman, A. King, S. Chen, C. Zhang, H. Tan, Robots under COVID-19 pandemic: A comprehensive survey. *IEEE Access* **9**, 1590–1615 (2021).
- G.-Z. Yang, B. J. Nelson, R. R. Murphy, H. Choset, H. Christensen, S. H. Collins, P. Dario, K. Goldberg, K. Ikuta, N. Jacobstein, D. Kragic, R. H. Taylor, M. McNutt, Combating COVID-19—The role of robotics in managing public health and infectious diseases. *Sci. Robot.* **5**, eabb5589 (2020).
- T. R. Ray, J. Choi, A. J. Bhandokar, S. Krishnan, P. Gutruf, L. Tian, R. Ghaffari, J. A. Rogers, Bio-integrated wearable systems: A comprehensive review. *Chem. Rev.* **119**, 5461–5533 (2019).
- D. H. Kim, N. Lu, R. Ma, Y. S. Kim, R. H. Kim, S. Wang, J. Wu, S. M. Won, H. Tao, A. Islam, K. J. Yu, T. I. Kim, R. Chowdhury, M. Ying, L. Xu, M. Li, H. J. Chung, H. Keum, M. McCormick, P. Liu, Y. W. Zhang, F. G. Omenetto, Y. Huang, T. Coleman, J. A. Rogers, Epidermal electronics. *Science* **333**, 838–843 (2011).
- W. Gao, S. Emaminejad, H. Y. Nyein, S. Challa, K. Chen, A. Peck, H. M. Fahad, H. Ota, H. Shiraki, D. Kiriya, D.-H. Lien, G. A. Brooks, R. W. Davis, A. Javey, Fully integrated wearable sensor arrays for multiplexed in situ perspiration analysis. *Nature* **529**, 509–514 (2016).
- Y. Yang, Y. Song, X. Bo, J. Min, O. S. Pak, L. Zhu, M. Wang, J. Tu, A. Kogan, H. Zhang, T. K. Hsiai, Z. Li, W. Gao, A laser-engraved wearable sensor for sensitive detection of uric acid and tyrosine in sweat. *Nat. Biotechnol.* **38**, 217–224 (2020).
- B. Shih, D. Shah, J. Li, T. G. Thuruthel, Y.-L. Park, F. Iida, Z. Bao, R. Kramer-Bottiglio, M. T. Tolley, Electronic skins and machine learning for intelligent soft robots. *Sci. Robot.* **5**, eaaz9239 (2020).
- Y. Yu, J. Nassar, C. Xu, J. Min, Y. Yang, A. Dai, R. Doshi, A. Huang, Y. Song, R. Gehlhar, A. D. Ames, W. Gao, Biofuel-powered soft electronic skin with multiplexed and wireless sensing for human-machine interfaces. *Sci. Robot.* **5**, eaaz7946 (2020).
- T. Someya, Z. Bao, G. G. Malliaras, The rise of plastic bioelectronics. *Nature* **540**, 379–385 (2016).
- C. Wang, X. Li, H. Hu, L. Zhang, Z. Huang, M. Lin, Z. Zhang, Z. Yin, B. Huang, H. Gong, S. Bhaskaran, Y. Gu, M. Makihata, Y. Guo, Y. Lei, Y. Chen, C. Wang, Y. Li, T. Zhang, Z. Chen, A. P. Pisano, L. Zhang, Q. Zhou, S. Xu, Monitoring of the central blood pressure waveform via a conformal ultrasonic device. *Nat. Biomed. Eng.* **2**, 687–695 (2018).
- J. Kim, A. S. Campbell, B. E.-F. de Ávila, J. Wang, Wearable biosensors for healthcare monitoring. *Nat. Biotechnol.* **37**, 389–406 (2019).
- S. Choi, S. I. Han, D. Jung, H. J. Hwang, C. Lim, S. Bae, O. K. Park, C. M. Tschabrunn, M. Lee, S. Y. Bae, J. W. Yu, J. H. Ryu, S.-W. Lee, K. Park, P. M. Kang, W. B. Lee, R. Nezafat, T. Hyeon, D.-H. Kim, Highly conductive, stretchable and biocompatible Ag–Au core–Sheath nanowire composite for wearable and implantable bioelectronics. *Nat. Nanotech.* **13**, 1048–1056 (2018).
- K. Sim, F. Ershad, Y. Zhang, P. Yang, H. Shim, Z. Rao, Y. Lu, A. Thukral, A. Elgalad, Y. Xi, B. Tian, D. A. Taylor, C. Yu, An epicardial bioelectronic patch made from soft rubbery materials and capable of spatiotemporal mapping of electrophysiological activity. *Nat. Electron.* **3**, 775–784 (2020).
- A. S. Almuslem, S. F. Shaikh, M. M. Hussain, Flexible and stretchable electronics for harsh-environmental applications. *Adv. Mater. Technol.* **4**, 1900145 (2019).
- Y.-T. Kwon, Y.-S. Kim, S. Kwon, M. Mahmood, H.-R. Lim, S.-W. Park, S.-O. Kang, J. J. Choi, R. Herbert, Y. C. Jang, Y.-H. Choa, W.-H. Yeo, All-printed nanomembrane wireless bioelectronics using a biocompatible solderable graphene for multimodal human-machine interfaces. *Nat. Commun.* **11**, 3450 (2020).
- A. J. Bhandokar, S. P. Lee, I. Huang, W. Li, S. Wang, C.-J. Su, W. J. Jeang, T. Hang, S. Mehta, N. Nyberg, P. Gutruf, J. Choi, J. Koo, J. T. Reeder, R. Tseng, R. Ghaffari, J. A. Rogers, Sweat-activated biocompatible batteries for epidermal electronic and microfluidic systems. *Nat. Electron.* **3**, 554–562 (2020).



31. Z. Zhou, K. Chen, X. Li, S. Zhang, Y. Wu, Y. Zhou, K. Meng, C. Sun, Q. He, W. Fan, E. Fan, Z. Lin, X. Tan, W. Deng, J. Yang, J. Chen, Sign-to-speech translation using machine-learning-assisted stretchable sensor arrays. *Nat. Electron.* **3**, 571–578 (2020).
32. B. Ciui, A. Martin, R. K. Mishra, T. Nakagawa, T. J. Dawkins, M. Lyu, C. Cristea, R. Sandulescu, J. Wang, Chemical sensing at the robot fingertips: Toward automated taste discrimination in food samples. *ACS Sens.* **3**, 2375–2384 (2018).
33. M. Amit, R. K. Mishra, Q. Hoang, A. M. Galan, J. Wang, T. N. Ng, Point-of-use robotic sensors for simultaneous pressure detection and chemical analysis. *Mater. Horiz.* **6**, 604–611 (2019).
34. A. K. S. Kumar, Y. Zhang, D. Li, R. G. Compton, A mini-review: How reliable is the drop casting technique? *Electrochem. Commun.* **121**, 106867 (2020).
35. A. Moin, A. Zhou, A. Rahimi, A. Menon, S. Benatti, G. Alexandrov, S. Tamakloe, J. Ting, N. Yamamoto, Y. Khan, F. Burghardt, L. Benini, A. C. Arias, J. M. Rabaey, A wearable biosensing system with in-sensor adaptive machine learning for hand gesture recognition. *Nat. Electron.* **4**, 54–63 (2021).
36. S. Guo, D. Wen, Y. Zhai, S. Dong, E. Wang, Platinum nanoparticle ensemble-on-graphene hybrid nanosheet: One-pot, rapid synthesis, and used as new electrode material for electrochemical sensing. *ACS Nano* **4**, 3959–3968 (2010).
37. D. Troya, Reaction mechanism of nerve-agent decomposition with Zr-based metal organic frameworks. *J. Phys. Chem. C* **120**, 29312–29323 (2016).
38. M. C. de Koning, M. van Grol, T. Breijjaert, Degradation of paraoxon and the chemical warfare agents VX, tabun, and soman by the metal–organic frameworks UiO-66-NH<sub>2</sub>, MOF-808, NU-1000, and PCN-777. *Inorg. Chem.* **56**, 11804–11809 (2017).
39. J. Wang, Carbon-nanotube based electrochemical biosensors: A review. *Electroanalysis* **17**, 7–14 (2005).
40. V. Schroeder, S. Savagatrup, M. He, S. Lin, T. M. Swager, Carbon nanotube chemical sensors. *Chem. Rev.* **119**, 599–663 (2019).
41. R. M. Torrente-Rodríguez, H. Lukas, J. Tu, J. Min, Y. Yang, C. Xu, H. B. Rossiter, W. Gao, SARS-CoV-2 RapidPlex: A graphene-based multiplexed telemedicine platform for rapid and low-cost COVID-19 diagnosis and monitoring. *Matter* **3**, 1981–1998 (2020).
42. S. M. Lundberg, S.-I. Lee, A unified approach to interpreting model predictions. *Adv. Neural Inf. Process. Syst.* **2017**, 4765–4774 (2017).
43. B. Hudgins, P. Parker, R. N. Scott, A new strategy for multifunction myoelectric control. *I.E.E.E. Trans. Biomed. Eng.* **40**, 82–94 (1993).
44. R. A. Russell, D. Thiel, R. Deveza, A. Mackay-Sim, A robotic system to locate hazardous chemical leaks. *IEEE Int. Conf. Robot. Autom.* **1**, 556–561 (1995).
45. X. Liu, D. Gong, A comparative study of A-star algorithms for search and rescue in perfect maze, in *Proceedings of the 2011 International Conference on Electric Information and Control Engineering* (IEEE, 2011), Wuhan, 15 to 17 April 2011, pp. 24–27.
46. W. S. Hummers, R. E. Offeman, Preparation of graphitic oxide. *J. Am. Chem. Soc.* **80**, 1339 (1958).
47. J. G. Yoon, J. Yoon, J. Y. Song, S.-Y. Yoon, C. S. Lim, H. Seong, J. Y. Noh, H. J. Cheong, W. J. Kim, Clinical significance of a high SARS-CoV-2 viral load in the saliva. *J. Korean Med. Sci.* **35**, e195 (2020).

**Acknowledgments:** We acknowledge critical support and infrastructure provided for this work by the Kavli Nanoscience Institute at Caltech. J.T. was supported by the National Science Scholarship from the Agency for Science, Technology and Research (A\*STAR), Singapore.

**Funding:** This work was supported by National Institutes of Health grant R01HL155815 (W.G.), Office of Naval Research grant N00014-21-1-2483 (W.G.), Translational Research Institute for Space Health grant NASA NNX16AO69A (W.G.), Tobacco-Related Disease Research Program grant R01RG3746 (W.G.), and Carver Mead New Adventures Fund at California Institute of Technology (W.G.). **Author contributions:** Conceptualization: W.G. and Y.Y. Methodology: Y.Y., J.L., and S.A.S. Investigation: Y.Y., J.L., S.A.S., J.M., J.T., W.G., C.X., and Y.S. Funding acquisition: W.G. Supervision: W.G. Writing—original draft: W.G., Y.Y., J.L., and S.A.S. Writing—review and editing: J.T., W.G., C.X., and Y.S. **Competing interests:** The authors declare that they have no competing interests. **Data and materials availability:** All data needed to support the conclusions of this manuscript are included in the main text or Supplementary Materials. The code for this study is available at <https://github.com/Samwich1998/Robotic-Arm> (sEMG-based robotic arm control) and <https://github.com/Samwich1998/Boat-Search-Algorithm> (M-Boat search algorithm).

Submitted 30 October 2021

Accepted 10 May 2022

Published 1 June 2022

10.1126/scirobotics.abn0495

## All-printed soft human-machine interface for robotic physicochemical sensing

You YuJiahong LiSamuel A. SolomonJihong MinJiaobing TuWei GuoChanghao XuYu SongWei Gao

*Sci. Robot.*, 7 (67), eabn0495. • DOI: 10.1126/scirobotics.abn0495

### View the article online

<https://www.science.org/doi/10.1126/scirobotics.abn0495>

### Permissions

<https://www.science.org/help/reprints-and-permissions>

Use of this article is subject to the [Terms of service](#)

---

*Science Robotics* (ISSN ) is published by the American Association for the Advancement of Science, 1200 New York Avenue NW, Washington, DC 20005. The title *Science Robotics* is a registered trademark of AAAS.

Copyright © 2022 The Authors, some rights reserved; exclusive licensee American Association for the Advancement of Science. No claim to original U.S. Government Works